Raman spectroscopy of graphene and related materials

Anna K Ott[a] **and Andrea C Ferrari**[b], [a]NS3E Laboratory, UMR 3208 ISL/CNRS/UNISTRA, French-German Research Institute of Saint-Louis, Saint Louis, France; [b]Cambridge Graphene Centre, University of Cambridge, Cambridge, United Kingdom

Abstract

Raman spectroscopy is one of the main characterization techniques for graphene and related materials. It is a non-destructive technique that can give insight in the material's quality, the number of layers, and is sensitive to any changes in electric or magnetic fields, band structure and temperature, making it ideal to probe layered materials.

Key points

- Brief introduction to Raman scattering
- Explanation of the Raman spectrum of graphene/graphene layers and how it changes as function of doping, defects, and strain
- Summary of the capabilities of Raman spectroscopy of graphene
- Overview of the current challenges and general outlook

Introduction

A single layer of graphene (SLG) (Novoselov et al., 2004) can be seen by using a microscope if placed over a Si+SiO_2 thickness ~100 nm or ~ 300 nm (Casiraghi et al., 2007a). The SiO_2 layer acts as a cavity for the light and results in either constructive or destructive interference depending on its thickness (Casiraghi et al., 2007a). Fig. 1 shows the calculated optical contrast as function of laser wavelength and SiO_2 thickness with contrast maxima at ~100 and ~ 300 nm thickness for commonly used laser wavelengths between ~450 and ~ 600 nm. While imaging by optical contrast can give an idea of its thickness, it is not enough to get more quantitative information, such as doping, disorder, strain, etc.

Raman spectroscopy is a powerful characterization technique for carbons in general, ranging from fullerenes, nanotubes, graphitic carbons to amorphous and diamond-like carbons (Ferrari and Robertson, 2000; Tuinstra and Koenig, 1970; Dresselhaus et al., 2005; Dresselhaus et al., 1996). In graphene, Raman spectroscopy can now be routinely used to extract the number of layers, N, to estimate the type and amount of doping and strain, as well as to check the quality of graphene as it this spectroscopic technique is also sensitive to defects (Ferrari and Basko, 2013).

Brief overview of light scattering processes

Light scattering can be either elastic, i.e. the incident and scattered light have the same frequency, or inelastic, where the scattered light has a different frequency with respect to the incident light. In classical electrodynamics, when light impinges on a medium, electrons within that medium start to oscillate at the same frequency as the incident electromagnetic wave. This periodic perturbation of the electron cloud results in the creation of an oscillating dipole moment leading to the emission of light with the same frequency as the incident light, i.e. elastic scattering of light. Examples are Mie scattering (Mie, 1908) and Rayleigh

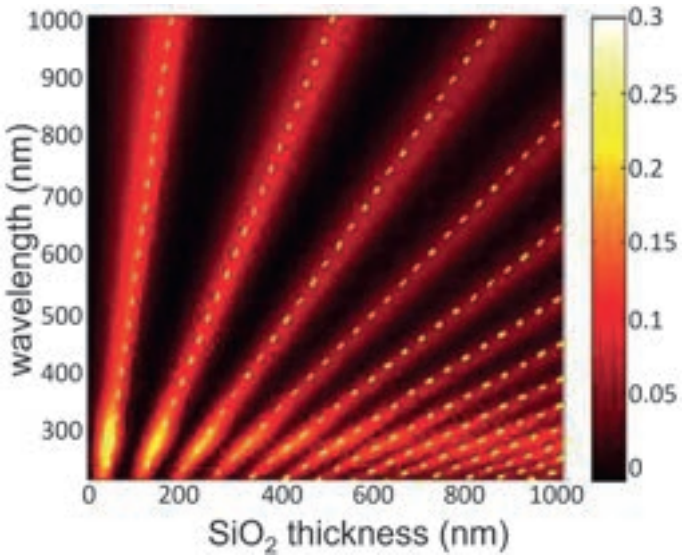

Fig. 1 Calculated optical contrast of graphene on Si/SiO_2 as a function of wavelength and SiO_2 thickness. Reprinted with permission from Casiraghi C, Hartschuh A, Lidorikis E, Qian H, Harutyunyan H, Gokus T, Novoselov KS, and Ferrari AC (2007a) Rayleigh imaging of graphene and graphene layers. *Nano Letters* 7: 2711–2717. Copyright 2007 American Chemical Society.

scattering (Strutt, 1871), depending on the particle size in the medium. Light scattering off particles larger than the wavelength and having a refractive index different from that of the continuous medium in which they are embedded is referred to as Mie scattering, which can be observed when sun light scatters from the water droplets within clouds. If the particle size is smaller than the wavelength of light, such as is the case for atoms or molecules, the process is called Rayleigh scattering. An example is the color of the sky, either blue during the day or red at sun rise or sunset, where light is scattered off the molecules in the atmosphere.

In the case of inelastic light scattering, the scattered light has a different frequency or energy with respect to the incident light. This process can be more conveniently described by quantum theory, whereas an electron absorbs a photon, leaving behind an empty space (a hole), and as a result is promoted to an energetically higher level. The electron can then either fall directly back to a lower level, while emitting a photon with energy corresponding to the energy level difference, or scatter with the lattice, i.e. create or annihilate/absorb a phonon, before recombining radiatively with a hole. Examples for inelastic light scattering are Brillouin and Raman scattering. While Brillouin scattering involves low frequency lattice vibrations, i.e. acoustic phonons, Raman scattering involves optical phonons in first order scattering processes (Brüesch, 1986).

The Raman scattering process was first theoretically predicted in 1923 by Austrian physicist Smekal (Smekal, 1923). The experimental proof was delivered in 1928 by Landsberg and Mandelstam (Landsberg and Mandelstam, 1928) in crystals and by Raman and Krishnan (Raman and Krishnan, 1928) in liquids. For his findings Raman was awarded the Nobel Prize in physics in 1930 (Nobel-Prize). Since then - and even more so after the invention of the laser in 1960 (Schawlow and Townes, 1958; Maiman, 1960) - Raman spectroscopy has become a standard materials characterization tool as it is non-destructive, fast and easy to use (Ferrari and Basko, 2013).

Raman scattering process

Raman scattering is the inelastic scattering between light, i.e. a photon, and matter. It involves the exchange of rotational or vibrational quanta of energy in molecules or the creation and annihilation of phonons with frequency Ω in solids (Cardona and Güntherodt, 1982). If light of frequency ω_L is incident on a material, most of the light is elastically scattered. This Rayleigh scattering process is shown in Fig. 2. From a classical point of view, light can be described as a propagating electromagnetic wave with $E(t) = E_0 \cos(\omega_L t)$ with amplitude E_0 and frequency ω_L. The electron cloud responds to the fast changing electric field and this will induce a dipole moment $\mu(t)$ proportional to the electric field of the incoming light (Yu and Cardona, 1996):

$$\mu(t) = \alpha E(t) = \alpha_0 E_0 \cos(\omega_L t) \quad (1)$$

where the proportionality constant α is the polarizability. This describes the ability of, e.g., molecules to be polarized, and depends on the relative position of the individual atoms. Atomic vibrations are confined to certain energetic levels and are quantized into phonons. The physical displacement of the atoms dQ about their equilibrium position associated with a phonon can be described as: $dQ = Q_0 \cos(\Omega t)$, where Ω is the phonon frequency and Q_0 is the displacement about the equilibrium position. A material's response to electromagnetic radiation depends on the atomic positions. The atomic displacements change the susceptibility, thus its polarization, depending on the phonon involved. At room temperature (RT) the atomic displacement is small

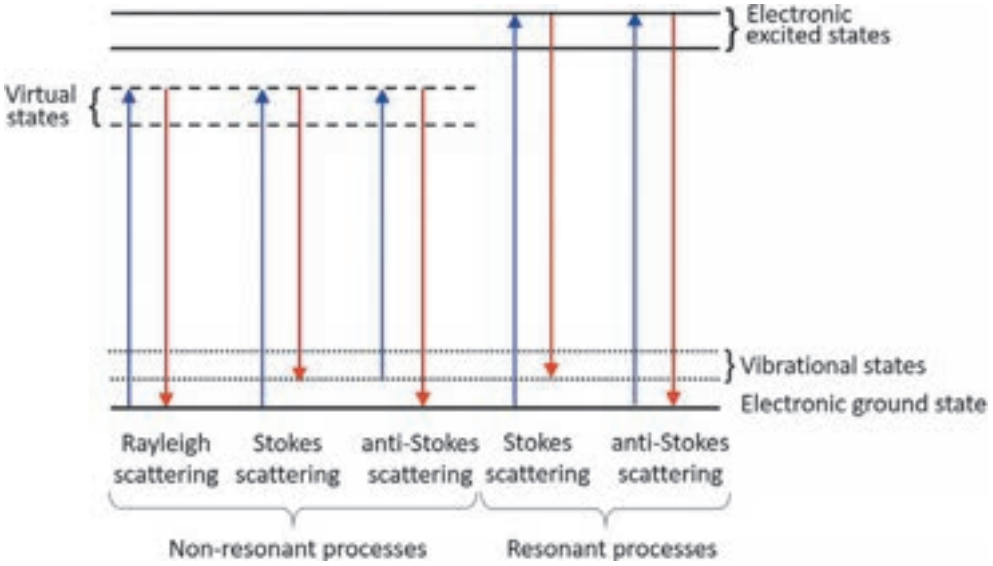

Fig. 2 Energy level diagram showing Rayleigh and Raman scattering (Stokes and anti-Stokes) processes. Blue lines depict absorption of a photon, while red lines depict emission of a photon. Non-resonant processes involve virtual states, while resonant scattering processes involve real states.

compared to the lattice constant. Therefore, the polarizability α can be approximated by a Taylor series expansion around the lattice displacement. Considering only first order terms we get:

$$\alpha = \alpha_0 + \left.\frac{\partial\alpha}{\partial Q}\right|_0 dQ + \ \ldots = \alpha_0 + \left.\frac{\partial\alpha}{\partial Q}\right|_0 Q_0 \cos(\Omega t) \tag{2}$$

Inserting Eq. (2) in (1) gives:

$$\mu(t) = \alpha_0 E_0 \cos(\omega_L\, t) + \left.\frac{\partial\alpha}{\partial Q}\right|_0 E_0 Q_0 \cos(\Omega t)\cos(\omega_L t)$$

Using a trigonometric identity for the product of the cosine terms leads to

$$\mu(t) = \alpha_0 E_0 \cos(\omega_L\, t) + \frac{1}{2}\left.\frac{\partial\alpha}{\partial Q}\right|_0 E_0 Q_0 \{\cos[(\Omega - \omega_L)t] + \cos[(\Omega + \omega_L)t]\} \tag{3}$$

The intensity of the scattered light I_{Sc} is proportional to $|\ddot{\mu}|$, where $\ddot{\mu}$ is the second derivative of μ with respect to time, t:

$$I_{Sc} \propto \cos^2(\omega_L) + \cos^2[(\omega_L + \Omega)t\,] + \cos^2[(\omega_L - \Omega)t\,] + \text{cross terms} \tag{4}$$

The first term corresponds to the *elastically* scattered light, i.e. Rayleigh scattering, since it only depends on ω_L,while the other two terms describe the inelastically scattered light, i.e. Raman scattering. Here we distinguish between Stokes (S) and anti-Stokes (AS) scattering, both named after Sir G. G. Stokes (Larmor, 1907). In S-scattering a phonon is created by energy transfer from the electron to the lattice resulting in the $(\omega_L - \Omega)$ term, meaning the scattered light has a lower frequency with respect to the incident light, while in AS-scattering a phonon is annihilated (or absorbed), giving the $(\omega_L + \Omega)$ term. The S and AS Raman scattering processes are depicted in Fig. 2. AS Raman scattering involves the absorption of a phonon. Consequently, the scattering process starts directly from a vibrational state as shown in Fig. 2.

At RT the AS-Raman peaks have lower intensity compared to S, but their intensity increases with rising temperature (T). This can be explained by considering the Bose-Einstein distribution, whereby the number of phonons in a certain energy state strongly depends on T, and increases with T (Kittel, 2005). If n_q is the phonon occupation number, then the S-Raman scattering intensity will be proportional to $n_q + 1$, since a phonon is created during the scattering process. For AS, we start at an excited (vibrational) state and a phonon is annihilated, giving rise to intensity proportional to n_q. Thus, the S/AS intensity ratio can be expressed as (Placzek, 1934; Krishnan and Narayanan, 1950):

$$\frac{I_{Stokes}}{I_{anti-Stokes}} = \left(\frac{\omega_L - \Omega}{\omega_L + \Omega}\right)^4 \exp\left(\frac{\hbar\Omega}{k_B T}\right), \tag{5}$$

where k_B is the Boltzmann constant, ω_L is the frequency of the laser light, Ω is the phonon frequency, $\hbar$ is the reduced Planck constant. By re-arranging Eq. (5) for T, the sample T can be determined by fitting the peak intensity of a peak on S and AS side of the Raman spectrum.

The intensity of the scattered light also strongly depends on whether we have a resonant or non-resonant process (Loudon, 1965). In a resonant process, real electronic states are involved, while in non-resonant Raman scattering virtual states are used to

describe the process. The intensity of the Raman scattered light depends on the polarization of the incident and scattered light as well as on the phonon involved in the scattering process. The symmetry of the phonon mode is incorporated in the so-called Raman tensor $\Re$. Introducing a unit vector in direction of the lattice displacement $\widehat{Q}$ this term can be expressed as (Yu and Cardona, 1996)

$$\Re = \left.\frac{\partial \alpha}{\partial Q}\right|_0 \widehat{Q} \tag{6}$$

Assuming $\widehat{e}_i$ and $\widehat{e}_{Sc}$ to be unit vectors of the polarization of the incoming and scattered light, the Raman intensity is proportional to $I \propto |\widehat{e}_i \, \Re \, \widehat{e}_{Sc}|^2$ (Yu and Cardona, 1996). Thus, for Raman scattering to occur, the term $\left.\frac{\partial \alpha}{\partial Q}\right|_0$ has to be non-zero, meaning the polarizability has to change. By doing polarization dependent measurements, the symmetry of the Raman tensor, thus that of the corresponding phonon, can be obtained (Cardona and Güntherodt, 1982). This is very useful for correct assignment of the Raman peaks.

During the scattering process, energy and momentum conservation have to hold: $\hbar\omega_L = \hbar\omega_{Sc} \pm \hbar\Omega$ and $\boldsymbol{k}_L = \boldsymbol{k}_{Sc} \pm \boldsymbol{q}$, where $\hbar$ is the reduced Planck constant, ω_L, ω_{Sc}, Ω are the frequency of the incident light, the scattered light and the phonon, respectively, and $\boldsymbol{k}_L$, $\boldsymbol{k}_{Sc}$, $\boldsymbol{q}$ are the corresponding wave vectors and the phonon momentum. The wavevectors can be expressed in terms of wavelength λ via $k = 2\pi\lambda^{-1}$. The lattice constant of a material is of the order of a few Å, thus much smaller than λ (in the order of a few hundreds of nm), giving k_L, $k_{Sc} \ll \pi a^{-1}$, which is the size of the first Brillouin zone (BZ), where a is the lattice constant. Combining this with the equations for energy and momentum conservation we can deduct that $q \ll \pi a^{-1}$ meaning $q \approx 0$. This is called the fundamental Raman selection rule, and tells us that the phonons contributing to first order Raman scattering stem from the BZ center. For higher order scattering processes, i.e. processes involving multiple phonons, the selection rule becomes $\sum \boldsymbol{q} = 0$. So, in a second order Raman process, two phonons with equal but opposite momentum are contributing since $\boldsymbol{q} + (-\boldsymbol{q}) = 0$.

Raman spectroscopy of graphene and graphene layers

In real space, single layer graphene (SLG) has a hexagonal structure resulting in a hexagonal structure in reciprocal space as well, where Γ marks the BZ center and the high symmetry points at the corner are labelled as **K** and **K′**, Fig. 3A. At these so-called Dirac points, SLG has a unique linear dispersion relation (Dirac cones).

In SLG there are two atoms per unit cell giving rise to six normal modes (two being doubly degenerate) at Γ with irreducible representation: $A_{2u} + B_{2g} + E_{1u} + E_{2g}$ (Nemanich et al., 1977). The E_{2g} and B_{2g} modes are both doubly degenerate, whereas the E_{2g} mode is Raman active and the B_{2g} is silent, i.e. neither Raman nor IR active (Nemanich et al., 1977). The A_{2u} and E_{1u} modes are both IR active modes (Ferrari and Basko, 2013).

The Raman spectrum of graphite and multilayer graphene consists of two different sets of peaks: those at higher wavenumbers, such as the D, G, 2D and 2D′ modes due to in-plane vibrations, and those at low frequency, such as the shear (C) and layer breathing modes (LBMs), due to the relative movement of the whole atomic planes, either parallel or perpendicular (Ferrari and Basko, 2013; Tan et al., 2012), Fig. 4. In SLG only the first set of peaks is visible (Ferrari et al., 2006).

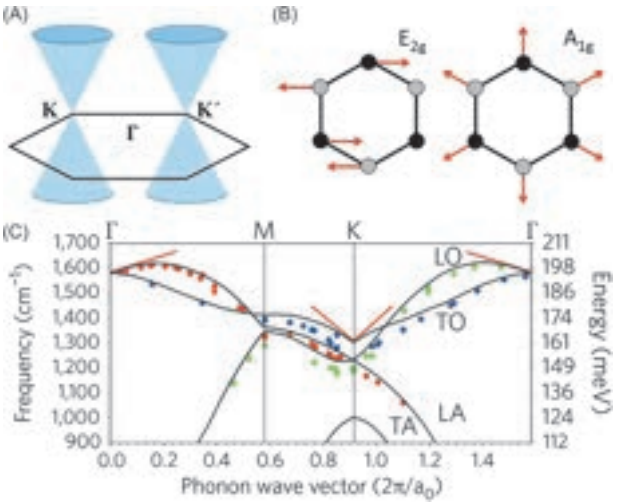

Fig. 3 (A) SLG structure in reciprocal space (BZ). The high symmetry points and a schematic of the electronic dispersion at K and K′ (Dirac cones) are indicated. (B) Doubly degenerate E_{2g} mode and A_{1g} breathing mode giving rise to the G and D peak in SLG. (C) SLG Phonon dispersion. The red lines indicate the positions of Kohn anomalies. (C) Reprinted with permission from Piscanec S, Lazzeri M, Mauri F, Ferrari AC, and Robertson J (2004) Kohn anomalies and electron-phonon interactions in graphite. *Physical Review Letters* 93: 185503. Copyright (2004) by the American Physical Society.

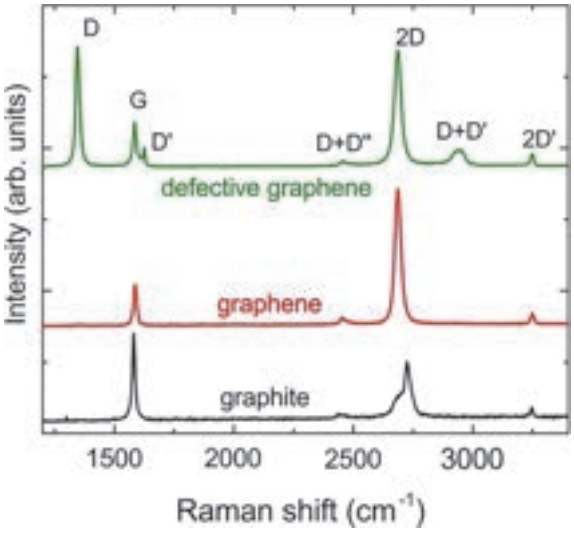

Fig. 4 Comparison of Raman spectra of pristine graphene, defective graphene and graphite.

The G peak ~1580 cm^{-1} arises from an E_{2g} phonon stemming from the Γ-point, Fig. 3B and C. The D peak, corresponding to an A_{1g} phonon (Fig. 3B), is due to the breathing mode of six-atom rings and requires a defect for its activation (Ferrari and Robertson, 2000; Thomsen and Reich, 2000; Tuinstra and Koenig, 1970) to fulfill the fundamental Raman selection rule. This peak is activated by an *inter*valley double resonance process (Thomsen and Reich, 2000), connecting **K** and **K′**, and comes from a transverse optical (TO) phonon at the **K** point, Fig. 3C. Due to the presence of a Kohn anomaly (Piscanec et al., 2004), i.e. a damping of the phonon dispersion (red lines in Fig. 3C), it is also highly dispersive with excitation energy shifting by ~50 cm^{-1} eV^{-1} (Pocsik et al., 1998). Similarly, an *intra*valley double resonance scattering process at **K** or **K′** gives rise to another defect-activated peak, the D′ peak. In defective graphene also the combination mode D + D′ starts to appear. The 2D and 2D′ peaks are the second order modes of the D and D′ peak, where the momentum conservation is fulfilled by scattering of two phonons with opposite wave vectors. Thus, these peaks do not require defects for their activation and are always present in the Raman spectrum of graphene (Ferrari et al., 2006; Basko et al., 2009). This means that only the G peak in the Raman spectrum of graphene fulfills the fundamental Raman selection rule directly as its origin is at the center of the Brillouin zone where $\boldsymbol{q} = 0$. All scattering processes are depicted in Fig. 5.

Counting graphene layers: 2D peak and ultra-low frequency modes

The Raman peaks of graphene can be fitted with a Lorentzian line shape, which arises from a finite, homogeneous lifetime broadening. Here we use the following notation (Ferrari and Basko, 2013) to refer to the peak fitting parameters: 'I' for peak height (intensity), 'A' for peak area, 'Pos' for peak position and 'FWHM' for the full-width at half-maximum of the peak.

The Raman scattering process in SLG is always resonant due to its linear band structure. The band structure of SLG and multilayer graphene (MLG) is reflected in the shape of the 2D peak (Ferrari et al., 2006). In SLG, the 2D peak is one sharp peak that can be fitted with a single Lorentzian line, while in Bernal stacked bilayer graphene (BLG) it splits into four components following the evolution of the band structure, Fig. 6A and B. Thus, the 2D peak shape can be used to estimate N. However, beyond ~5–10 layers, the 2D peak will start looking like that of graphite, Fig. 6A, and the 2D peak shape cannot be used, alone, to estimate N correctly. Low frequency modes are far more sensitive to N, even beyond $N = 5$, Fig. 6C. For accuracy the resulting peak positions of C and/or LBMs can be calculated as the mean value of the fitted S/AS peak positions.

The C peak changes its position with N, Fig. 6D. Following a linear chain model where each layer is estimated as one mass coupled by a spring to the next mass (layer), the relation between the position of the C peak (in cm^{-1}) and N can be written as (Tan et al., 2012):

$$\mathrm{Pos}(C)_N = \frac{1}{\sqrt{2}\pi c}\sqrt{\frac{\alpha}{\mu}}\sqrt{1 + \cos\left(\frac{\pi}{N}\right)} \tag{7}$$

where the pre-factor $(1/\pi c)\sqrt{\alpha/\mu}$ corresponds to $\mathrm{Pos}(C)_\infty$ in graphite with $N \to \infty$, $\alpha \sim 12.8 \times 10^{18}$ Nm^{-3} is the interlayer coupling constant, $\mu = 7.6 \times 10^{-27} kgÅ^{-2}$ is the SLG mass per unit area and c is the speed of light in cm s^{-1}.

Thus, by knowing Pos(C) in bulk graphite one can extract the interlayer coupling constant, thus get fundamental information about the interaction between the layers. This model can be applied to all layered materials (LMs), see e.g. refs. (Pizzi et al., 2021; Zhang et al., 2013).

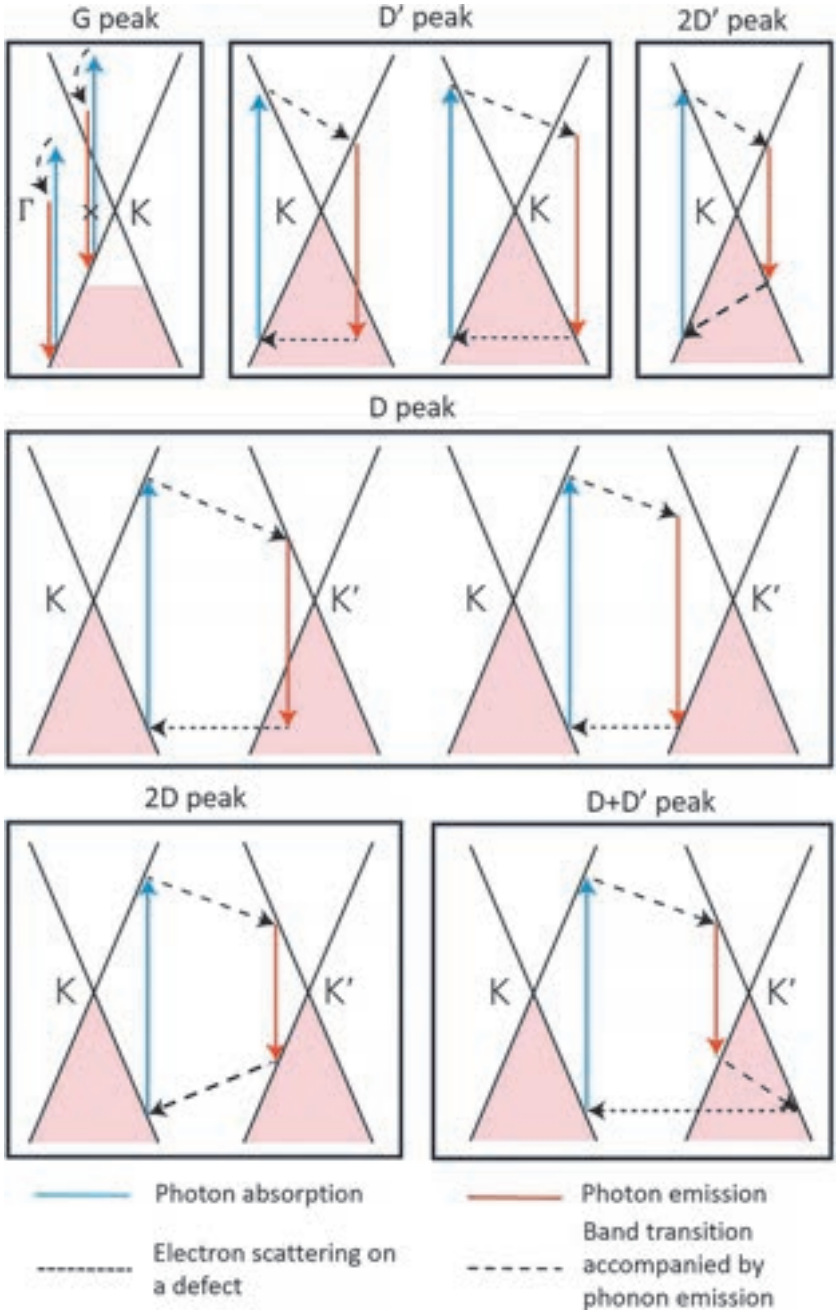

Fig. 5 Raman scattering processes in SLG. The red shaded area within the linear dispersion relation shows the occupied states. The G peak arises from one phonon scattering. Depending on doping, some processes will no longer be allowed. The D′ (intravalley scattering), D (intervalley scattering) and D + D′ peak require defects for their activation. The two different processes for the D and D′ peak depicted here give the largest contribution. The two-phonon (second order) modes, 2D and 2D' peak, do not require a defect. Schematics from Ref. Ferrari AC and Basko DM (2013) Raman spectroscopy as a versatile tool for studying the properties of graphene. *Nature Nanotechnology* 8: 235–246. Reprinted by permission from Springer Nature Customer Service Centre GmbH: Springer Nature, Nature Nanotechnology, COPYRIGHT (2013).

The Raman spectrum of strained graphene

SLG can be stretched up to at least ~20% without breaking (Bunch et al., 2007; Lee et al., 2008). Strain in graphene has not only a major effect on its structure but also on its Raman spectrum. Strain can occur in different forms: Uniaxial (Mohiuddin et al., 2009; Yoon et al., 2011; Mohr et al., 2010; Huang et al., 2010), i.e. strain along one direction, and biaxial strain, i.e. isotropic strain (Ding et al., 2010; Zabel et al., 2012; Metzger et al., 2010). Both types can either be applied as tensile or compressive.

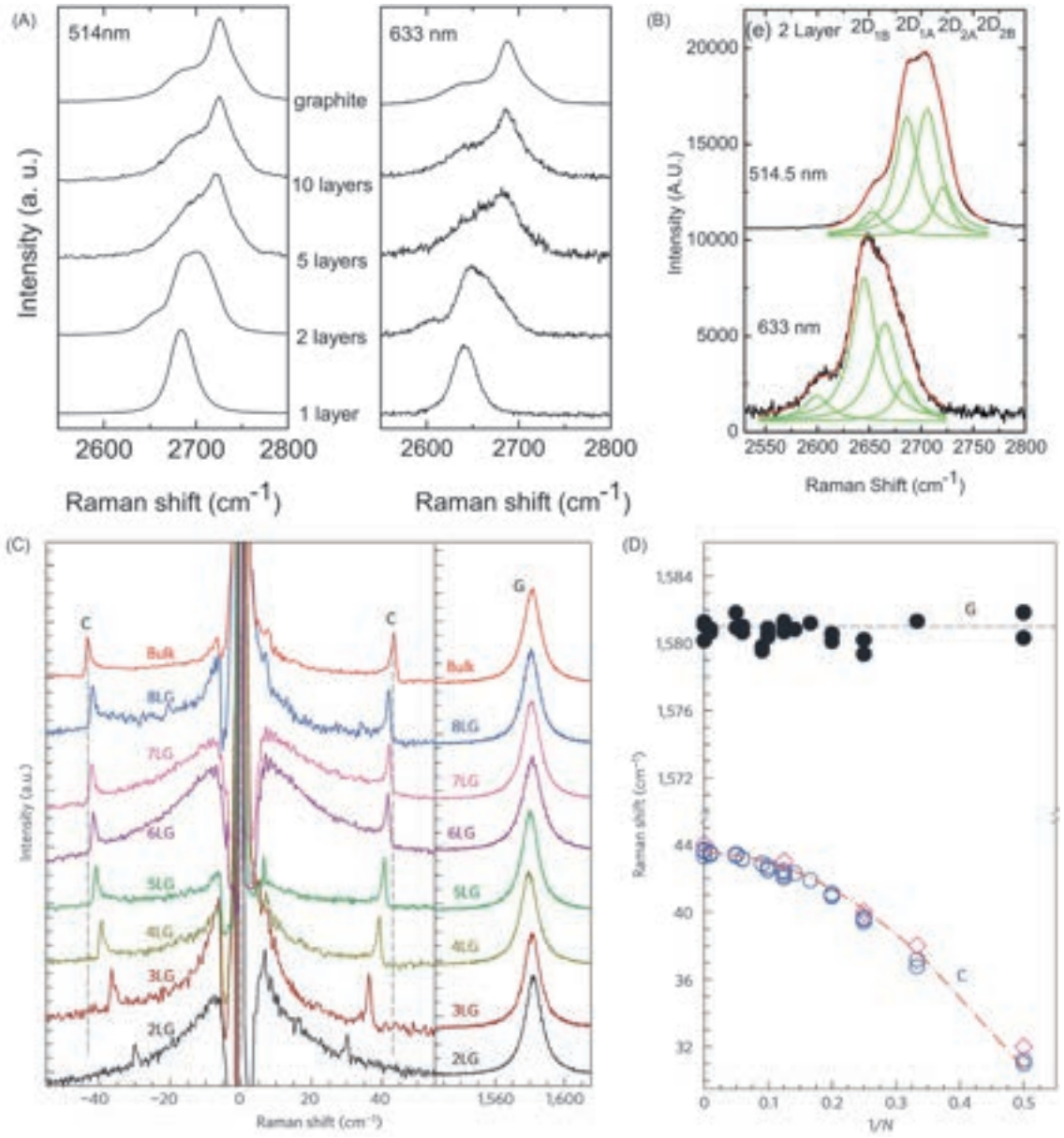

Fig. 6 (A) 2D peak as function N. (B) For BLG, the 2D peak splits into 4 components. (C) Ultra-low frequency and G peak region of graphene layers. (D) Fitted C and G peak positions. (A and B) Reprinted figure with permission from Ferrari AC, Meyer JC, Scardaci V, Casiraghi C, Lazzeri M, Mauri F, Piscanec S, Jiang D, Novoselov KS, Roth S, and Geim AK (2006) Raman spectrum of graphene and graphene layers. *Physical Review Letters* 97: 187401. Copyright (2006) by the American Physical Society. (C and D) From Springer Nature Customer Service Centre GmbH: Springer Nature, Nature Materials, Tan PH, Han WP, Zhao WJ, Wu ZH, Chang K, Wang H, Wang YF, Bonini N, Marzari N, Pugno N, Savini G, Lombardo A, and Ferrari AC (2012) The shear mode of multilayer graphene. *Nature Materials* 11: 294–300, COPYRIGHT (2012).

In general, compressive strain results in an upshift of all Raman peaks, arising from the shortening of the interatomic bond lengths, while tensile causes a downshift, due to the elongation of the bond lengths resulting in a weakening of the vibrational modes. Biaxial strain preserves the hexagonal symmetry in SLG, i.e. it only leads to an isotropic expansion or compression of the hexagonal lattice, resulting in a linear peak shift. The linear change in peak position or frequency $\partial\omega$ is $\partial\omega_G/\partial\varepsilon \approx -57$ cm^{-1}/% for the G peak and $\partial\omega_{2D}/\partial\varepsilon \approx -140$ cm^{-1}/% for the 2D peak (Zabel et al., 2012; Mohiuddin et al., 2009). Unless induced intentionally it is very unlikely to find biaxial strain in graphene samples. Uniaxial strain also results in linear peak shifts (Fig. 7), however it will break the hexagonal symmetry, which has an effect on the Raman peak shape. The G peak is a doubly degenerate mode and uniaxial strain makes both components visible: The peak splits into two components G^+ and G^-, one parallel and one perpendicular to the direction of applied strain (Mohiuddin et al., 2009), Fig. 7A–C. The rate of change is (Mohiuddin et al., 2009): $\partial\omega_{G^+}/\partial\varepsilon \approx -10.8$ cm^{-1}/% and $\partial\omega_{G^-}/\partial\varepsilon \approx -31.7$ cm^{-1}/% for the G peak and $\partial\omega_{2D}/\partial\varepsilon \approx -64$ cm^{-1}/% for the 2D peak. A similar splitting of the 2D peak has been reported when the uniaxial strain exceeds ~0.5% and is applied along a high-symmetry axis

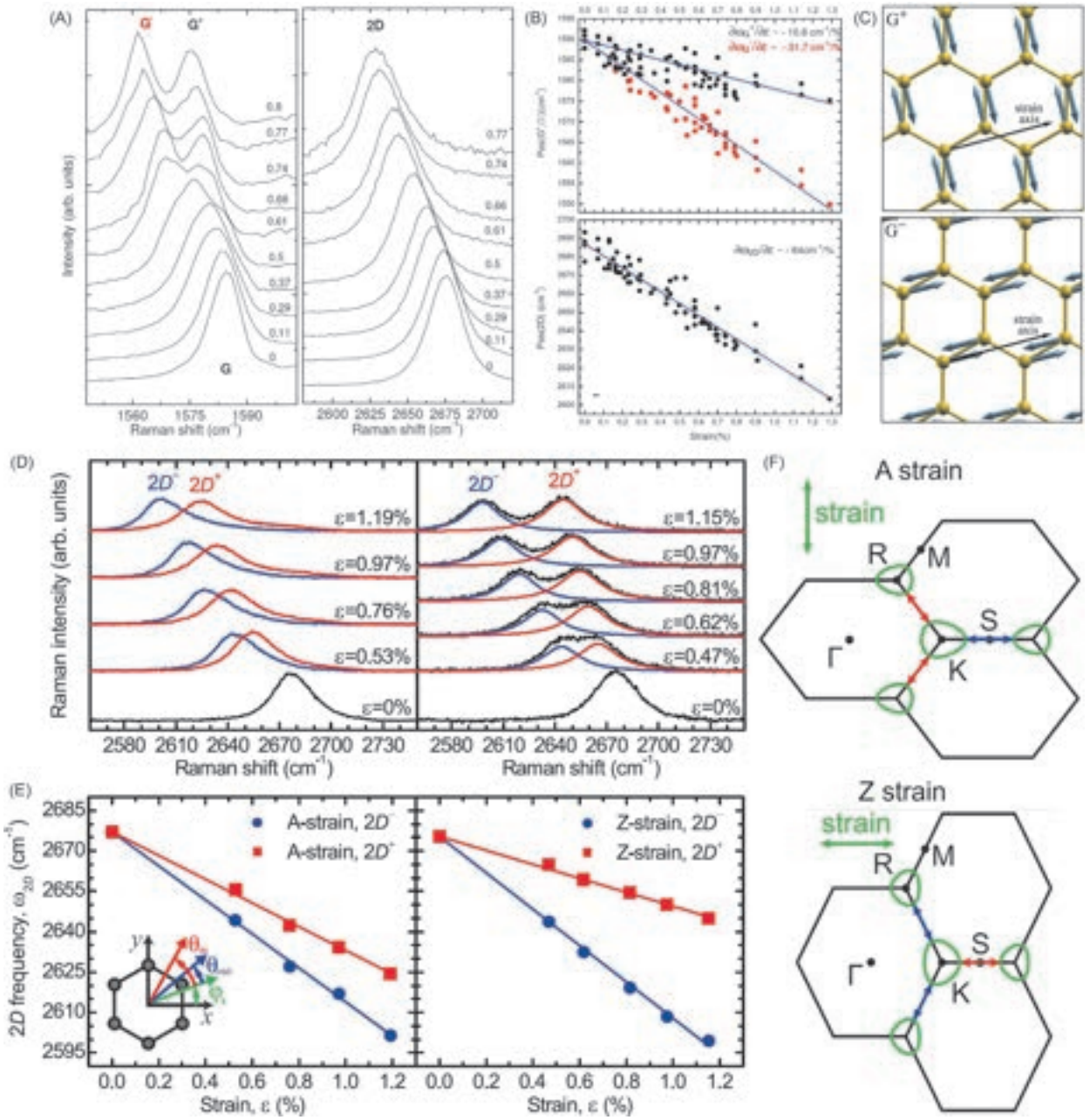

Fig. 7 Effect of uniaxial strain on the SLG Raman spectrum. (A) Splitting of the G peak and a linear peak shift for increasing uniaxial stain. (B) Fitted peak positions as function of strain. (C) Schematic showing the origin of the G peak splitting. Eigenvectors of G^+ and G^- modes, perpendicular and parallel to the strain direction. (D) Evolution of the 2D peak as function of strain. A splitting of the 2D peak can be observed. (E) Fitted peak positions as function of strain. (F) Schematics showing strain induced distortions of SLG and resulting change in distance between K and R (strained K′) points. (A, B, C) Reprinted figures with permission from Mohiuddin TMG, Lombardo A, Nair RR, Bonetti A, Savini G, Jalil R, Bonini N, Basko DM, Galiotis C, Marzari N, Novoselov KS, Geim AK, and Ferrari AC (2009) Uniaxial strain in graphene by Raman spectroscopy: G peak splitting, Gruneisen parameters, and sample orientation. *Physical Review B* 79: 205433. Copyright (2009) by the American Physical Society. (D, E, F) Reprinted figures with permission from Yoon D, Son Y-W, and Cheong H (2011) Strain-dependent splitting of the double-resonance Raman scattering band in graphene. *Physical Review Letters* 106: 155502. Copyright (2011) by the American Physical Society.

(Huang et al., 2010; Mohr et al., 2010; Yoon et al., 2011), Fig. 7D and E. The 2D peak arises from an intervalley scattering process connecting **K** and **K**′ points. Considering the structure of graphene, each **K** point has three neighboring **K**′ points, leading to three contributions to the scattering process. Fig.7F shows a schematic depicting the possible scattering processes for the 2D peak in strained graphene. The relative position of the Dirac points has been disturbed such that the three scattering mechanisms connecting **K** and **K**′ are no longer identical (Huang et al., 2010; Yoon et al., 2011). In the example shown in Fig. 7F two of the three possible scattering mechanism lead to one 2D peak component, while the remaining one gives rise to the second 2D peak component (red and blue arrows in Fig. 7F), depending on the direction of strain either parallel or perpendicular to the armchair edge in graphene.

The Raman spectrum of doped graphene

Most graphene samples produced by either micromechanical cleavage (MC), chemical vapor deposition (CVD), liquid phase exfoliation (LPE) or carbon segregation from SiC or metal substrates are doped due to the sensitivity of graphene to adsorbates, e.g. moisture, and/or due to the interaction with the underlying substrate (Bonaccorso et al., 2012; Backes et al., 2020). Doping can also be applied on purpose either electrically or chemically and has a marked effect on the Raman spectrum of (Basko et al., 2009; Das et al., 2008; Bruna et al., 2014; Kalbac et al., 2010; Casiraghi et al., 2007b): In doped SLG Pos(G) increases, while FWHM(G) decreases for both electron (e) and hole (h) doping, see Fig. 8A and C. The increase in Pos(G) is due to a non-adiabatic removal of the Kohn anomaly at Γ, while the decrease of FWHM(G) is due to Pauli blocking of the phonon decay channel into e-h pairs when the e-h gap is higher than the phonon energy, and saturates when the Fermi energy, E_F, is bigger than half the phonon energy (Basko et al., 2009; Das et al., 2008). The 2D peak, allows distinguishing between e and h doping, as Pos(2D) increases for h doping and decreases for e doping (Das et al., 2008), Fig. 8B. This can be explained by taking the change of the equilibrium lattice parameter into account with a consequent stiffening/softening of the phonon modes, as a result of h and e doping, respectively. Both, intensity and area ratios, I(2D)/I(G) and A(2D)/A(G) depend on E_F. The ratios are maximum for $E_F = 0$, and decrease with increasing E_F (Basko et al., 2009; Das et al., 2008), Fig. 8D. Using the fitting parameters Pos(G), FWHM(G), Pos(2D), I(2D)/I(G) and A(2D)/A(G) with the corresponding graphs as function of E_F presented in refs. (Basko et al., 2009, Das et al., 2008), E_F can be extracted from the Raman spectrum.

Additional effects occur for high doping levels ~0.9 eV. In this case an enhancement of the G peak intensity I(G) can be observed (Zhao et al., 2011). Doping changes the occupation of electronic states and since transitions from an empty state or to a filled state are impossible (Pauli exclusion principle), this can exclude some of the BZ regions from contributing to the Raman matrix element

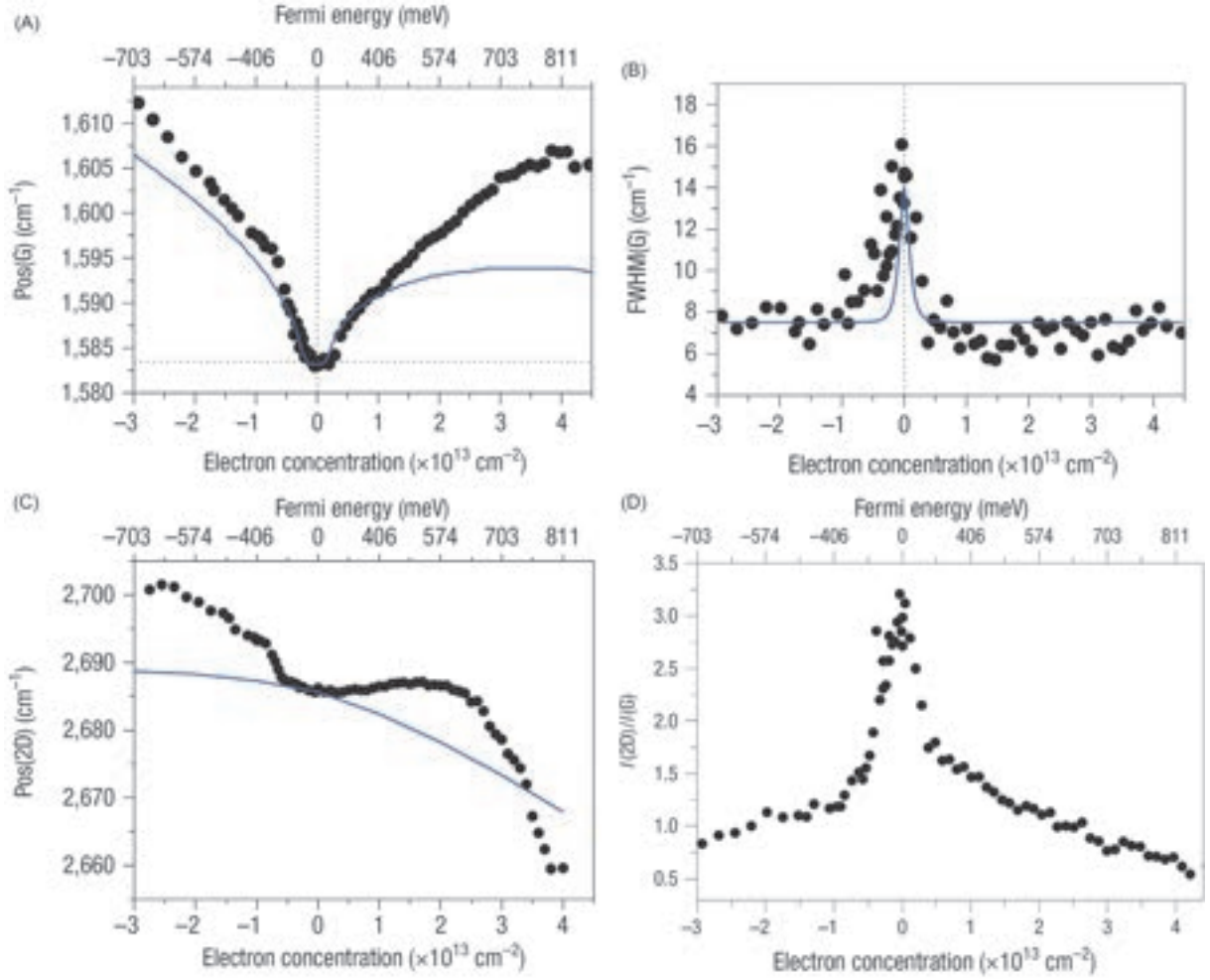

Fig. 8 (A) Pos(G), (B) Pos(2D), (C) FWHM(G) and (D) I(2D)/I(G) as function of doping. Reprinted by permission from Springer Nature Customer Service Centre GmbH: Nature/Springer, Nature Nanotechnology, Das A, Pisana S, Chakraborty B, Piscanec S, Saha SK, Waghmare UV, Novoselov KS, Krishnamurthy HR, Geim AK, Ferrari AC, and Sood AK (2008) Monitoring dopants by Raman scattering in an electrochemically top-gated graphene transistor. *Nature Nanotechnology* 3: 210–215. COPYRIGHT (2008).

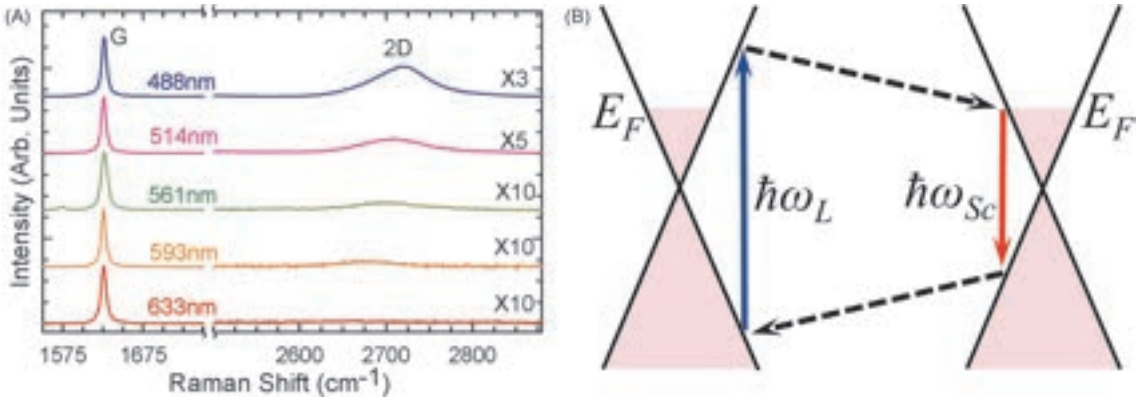

Fig. 9 Effect of high doping on the Raman spectrum of SLG. (A) The 2D peak is suppressed for certain excitation wavelengths. (B) Schematic of SLG band structure for e doped SLG, and 2D peak Raman scattering process. (A) Reprinted with permission from Zhao W, Tan PH, Liu J, and Ferrari AC (2011) Intercalation of few-layer graphite flakes with $FeCl_3$: Raman determination of fermi level, layer by layer decoupling, and stability. *Journal of the American Chemical Society* 133: 5941–5946. Copyright 2011 American Chemical Society; (B) Reprinted by permission from Springer Nature Customer Service Centre GmbH: Springer Nature, Nature Nanotechnology, Ferrari AC and Basko DM (2013) Raman spectroscopy as a versatile tool for studying the properties of graphene. Nature *Nanotechnology* 8: 235–246. COPYRIGHT (2013).

(Zhao et al., 2011). Because of suppression of destructive interference this leads to an enhancement of the G peak when $|E_F|$ matches half of the laser excitation energy $\hbar\omega_L/2$ (Zhao et al., 2011). At high doping the 2D peak is suppressed when the conduction band becomes filled at the energy probed by the laser (Zhao et al., 2011), Fig. 9A. There are 3 cases that can occur in highly doped samples (Ferrari and Basko, 2013): (i) the energy of the scattered (subscript 'Sc') and incoming photon (subscript 'L') are larger than twice E_F, i.e. $\omega_L, \omega_{Sc} > \frac{2E_F}{\hbar}$. in this case the 2D peak scattering mechanism is allowed, Fig. 9B; (ii) $\omega_{Sc} < 2|E_F|/\hbar < \omega_L$, the photon absorption is allowed but the phonon emission is excluded by Pauli blocking; (iii) $\omega_L, \omega_{Sc} < 2|E_F|/\hbar$ both photon absorption and phonon emission are blocked.

The Raman spectrum of defected graphene

There are many production methods for graphene, such as MC, CVD, LPE, etc. (Bonaccorso et al., 2012; Backes et al., 2020) and the quality may vary depending on the production technique. E.g. MC SLG is still thought to give the most intrinsic, defect-free and clean samples (Purdie et al., 2018). High quality samples with RT mobility~70,000 $cm^2V^{-1}\,s^{-1}$ in single crystal CVD and 30,000 $cm^2V^{-1}\,s^{-1}$ in polycrystalline CVD can be achieved by using optimized transfer processes (De Fazio et al., 2019). A measure for quality is the number of defects. Anything that breaks the hexagonal symmetry in graphene can be called a defect. Defects in graphene can occur as chemical adsorbates, edges or structural defects, such as vacancies. Perfect zig-zag edges in graphene cannot produce a D peak (Casiraghi et al., 2009; Cançado et al., 2004).

Raman spectroscopy in SLG is sensitive to defects and additional peaks appear. Ref. (Ferrari and Robertson, 2000) introduced a three-stage model of amorphisation going from stage 1: perfect SLG/graphite to nanocrystalline graphene, stage 2: nanocrystalline graphene to low-sp^3 amorphous carbon and stage 3: low-sp^3 amorphous carbon to highly disordered carbon, i.e. tetrahedral amorphous carbon. Here we will focus on stage 1, where the Raman spectrum evolves as follows:

1. The D peak appears and the ratio of D to G peak intensities, I(D)/I(G), increases
2. The D′ peak appears
3. All peaks broaden
4. The D + D′ peak appears
5. At the end of stage 1 the G and D′ peak are so wide that it is sometimes more convenient to consider them as a single, upshifted, wide G peak at 1600 cm^{-1}

Fig. 10 plots the evolution of the Raman spectrum of defected SLG within stage 1. A correlation between the intensity ratio I(D)/I(G) and the average crystal size L_a was first suggested by Tuinstra and Koenig (1970):

$$\frac{I(D)}{I(G)} = \frac{C(\lambda)}{L_a} \tag{8}$$

where C is a proportionality constant depending on the laser wavelength λ, and $C(514\text{ nm}) \sim 4.4$ nm (Tuinstra and Koenig, 1970; Knight and White, 1989).

Initially this was interpreted in terms of phonon confinement: the intensity of the forbidden process would be ruled by the 'amount of lifting' of the selection rule (Tuinstra and Koenig, 1970). Now we known that the D peak is produced only in a small region of the crystal near a defect or an edge (Casiraghi et al., 2009). For a nanocrystallite, I(G) is proportional to the sample area,

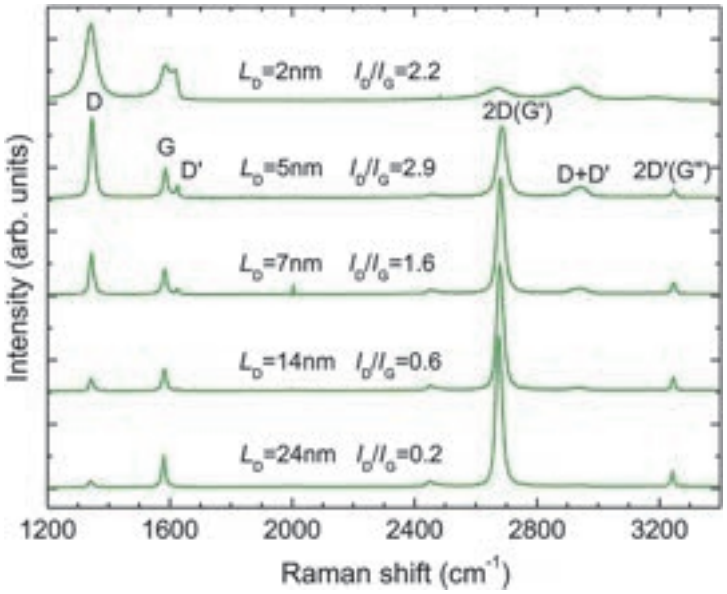

Fig. 10 Evolution of SLG Raman spectrum for increasing amount of defects (stage 1) introduced by Ar^+ bombardment. Reprinted with permission from Cançado LG, Jorio A, Ferreira EHM, Stavale F, Achete CA, Capaz RB, Moutinho MVO, Lombardo A, Kulmala TS, and Ferrari AC (2011) Quantifying defects in graphene via Raman spectroscopy at different excitation energies. *Nano Letters* 11: 3190–3196. Copyright 2011 American Chemical Society.

$\propto L_a^2$, while I(D) is proportional to the overall length of an edge, which scales as $\propto L_a$ (Ferrari and Basko, 2013) and thus $I(D)/I(G) \propto 1/L_a$. In stage 1, for a sample with defects, I(D) is proportional to the total number of defects probed by the laser spot. Therefore for an average interdefect distance L_D and laser spot size L_L there are on average $(L_L/L_D)^2$ defects in the area probed by the laser spot and $I(D) \propto (L_L/L_D)^2$ (Ferrari and Basko, 2013). On the other hand, I(G) is proportional to the total area probed by the laser spot $\propto L_L^2$, thus $I(D)/I(G) = C''(\lambda)/L_D^2$. This gives $C''(\lambda)/L_D^2 = I(D)/I(G) = C(\lambda)/L_a$ (Ferrari and Basko, 2013). However, for an increasing amount of defects the Tuinstra-Koenig relation will no longer hold (Ferrari and Robertson, 2000), as in this case $I(D)$ starts to decrease. The D peak is due to a breathing mode in 6-atoms rings (Ferrari and Robertson, 2000). With increasing amount of defects these rings will start to break and, as a result, I(D) will decrease, which is the onset of stage 2.

Taking the excitation energy dependence (E_L^4) of the Raman peak intensities into account, the following relation for the interdefect distance has been extracted (Cançado et al., 2011):

$$L_D^2[\mathrm{nm}^2] = \frac{(4.3 \pm 1.3) \times 10^3}{E_L^4\,[\mathrm{eV}^4]} \left(\frac{I(D)}{I(G)}\right)^{-1} \tag{9}$$

with the relation $n_D[\mathrm{cm}^{-2}] = 10^{14}/(\pi L_D^2)$, the defect concentration n_D can be related to I(D)/I(G) (Cançado et al., 2011):

$$n_D[\mathrm{cm}^{-2}] = (7.3 \pm 2.2) \times 10^9 E_L^4[\mathrm{eV}^4] \left(\frac{I(D)}{I(G)}\right) \tag{10}$$

Eqs. (9) and (10) can then be used directly to estimate the interdefect distance and corresponding defect concentration in SLG by calculating I(D)/I(G) from the fitted D and G peaks. These relations are limited to Raman active defects. Perfect zig-zag edges (Beams et al., 2011; Casiraghi et al., 2009), charged impurities (Casiraghi et al., 2007b; Das et al., 2008), intercalants (Zhao et al., 2011) and uniaxial or biaxial strain (Mohiuddin et al., 2009; Lee et al., 2008; Proctor et al., 2009; Zabel et al., 2012) do not generate a D peak. Other Raman signatures can be used for these 'silent' defects.

Eqs. (8) and (9) are valid for undoped SLG. However, most samples are not intrinsic and show $E_F \sim 200$–500 meV (Bruna et al., 2014). In the combined case of defects and doping a modified formula has to be used to correctly estimate the defect concentration and interdefect distance, due to the E_F dependence of I(D). (Bruna et al., 2014). Ref. Bruna et al. (2014) showed that I(D) decreases as E_F increases, Fig. 11, which would result in an underestimation of defects in doped SLG. By including the correction for the doping dependence of I(D), Eqs. (9) and (10) become (Bruna et al., 2014):

$$L_D^2[\mathrm{nm}^2] = \frac{(1.2 \pm 0.3) \times 10^3}{E_L^4\,[\mathrm{eV}^4]} \left(\frac{I(D)}{I(G)}\right)^{-1} \{E_F[eV]\}^{-(0.54\pm0.04)} \tag{11}$$

and

$$n_D[\mathrm{cm}^{-2}] = (2.7 \pm 0.8) \times 10^{10} E_L^4[\mathrm{eV}^4] \left(\frac{I(D)}{I(G)}\right) \{E_F[eV]\}^{(0.54\pm0.04)} \tag{12}$$

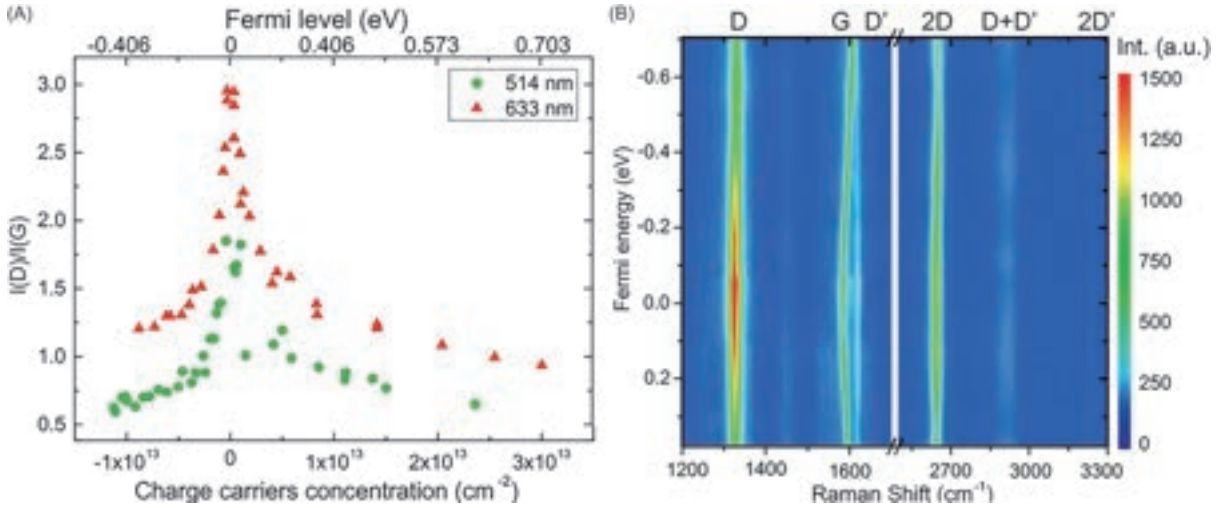

Fig. 11 (A) I(D)/I(G) as function of Fermi level E_F and charge carrier concentration. (B) Contour plot of the intensity of the Raman signal as function of E_F. Reprinted with permission from Bruna M, Ott AK, Ijäs M, Yoon D, Sassi U, and Ferrari AC (2014) Doping dependence of the Raman spectrum of defected graphene. *ACS Nano* 8: 7432–7441. Copyright 2014 American Chemical Society.

The doping dependence of the D peak intensity can be explained by taking the scattering rate or line broadening energy $\gamma = \hbar\tau^{-1}$ into account, where τ is the lifetime of an electronic state (Basko et al., 2009). In the presence of defects and doping the total scattering rate γ_{tot} is governed by electron-phonon interactions as well as scattering due to defects and e-e interactions, which in turn strongly depends on the E_F. It is given by (Bruna et al., 2014): $\gamma_{tot} = \gamma_{e-ph} + \gamma_D + \gamma_{ee}(E_F)$, where $\gamma_{ee}(E_F) = 0.06|E_F|$ (Basko et al., 2009). Thus, for increasing E_F, γ_{ee} will increase, and so will γ_{tot}. A higher scattering rate indicates a shorter lifetime, which, in turn, results in an increase in peak width and decrease in peak intensity. Eqs. (11) and (12) are valid for defects within stage 1 and for $E_F < E_L/2$ in order to avoid Pauli blocking (Bruna et al., 2014).

Magnetic fields

Magnetic fields have also an effect on the Raman spectrum of graphene. In the presence of a magnetic field, electronic trajectories will become circular, thus the backscattering condition of the Raman scattering process will be modified, such that the emitted phonons have smaller momenta (Ando, 2007; Goerbig et al., 2007). Ref. (Faugeras et al., 2010) observed a shift toward lower wavenumbers and a broadening of the 2D peak in SLG when applying a perpendicular magnetic field up to 30 T. In the presence of such a strong magnetic field the electronic states are quantized into discrete levels, called Landau levels (Kittel, 2005). Raman spectroscopy can also be used to probe those Landau levels and extract the Fermi velocity (Ferrari and Basko, 2013). Without magnetic field, electronic excitations in SLG have a continuous spectrum (Wallace, 1947). In the presence of a magnetic field, as result of this electronic quantization, inelastic scattering of photons occurs due to inter-Landau level transitions (Faugeras et al., 2011) resulting in sharp B-field dependent peaks where, instead of a phonon, an e-h pair is emitted (Kashuba and Fal'ko, 2012; Kashuba and Fal'ko, 2009; Mucha-Kruczyński et al., 2010). Applying magnetic fields can also be used to estimate the e-phonon coupling and probe the electronic Landau levels (Faugeras et al., 2011; Kim et al., 2012; Kossacki et al., 2011).

Key issues

While acquiring Raman spectra is not particularly difficult, the data analysis needs to be done considering the contribution of different influences, such as strain, doping, defects, etc. Instead of taking single point spectra, Raman measurements are often performed as mapping, where spectra are recorded in a grid pattern across areas of several $\sim\mu m^2$. Having a high spatial resolution is important for Raman mapping. The laser spot size, thus the spatial resolution, in conventional Raman spectroscopy is dictated by the diffraction limit of light, in turn proportional to the laser wavelength, thus of the order of $\sim$1 μm (Cardona and Güntherodt, 1982).

To analyze small flakes (<1 μm) with weak Raman signals, enhanced Raman scattering techniques, such as surface enhanced Raman scattering (SERS) (Kneipp et al., 2006) or tip-enhanced Raman scattering (TERS) can be used (Stöckle et al., 2000; Cao and Sun, 2022; Hartschuh et al., 2003). Both techniques exploit surface plasmons excited in metallic nanostructures by the incident radiation field of the laser, whereas in TERS the metallic nanostructure is provided by the apex of an atomic force microscopy tip

coated with a noble metal such as Au or Ag (Cao and Sun, 2022). With TERS, samples can be raster scanned with very high spatial resolution around tens of nm or less. Information can be derived combining topography with Raman at each raster point (Cao and Sun, 2022). SLG is ideal to study SERS effects of differently shaped and sized plasmonic nanostructures (Schedin et al., 2010; Lee et al., 2011). TERS has also been used to study twisted BLG (Gadelha et al., 2021), extracting the moiré wavelength and imaging different stacking regions (Gadelha et al., 2021). TERS can used for LMs in general, to identify local inhomogeneities, such as local strain, doping or defects (Malard et al., 2021; Rabelo et al., 2020).

Conclusion

We have given an overview of Raman scattering in graphene. We have discussed how Raman spectroscopy is sensitive to the number of layers and structural defects as well as external influences such as doping, strain and magnetic fields. Raman spectroscopy is a powerful technique to extract quantitative information about the quality of graphene, its doping, and type and amount of strain, crucial for further processing graphene for any kind of device (Backes et al., 2020). It is key for quality control when moving toward industrial scale production of graphene (Backes et al., 2020). Raman spectroscopy has also been employed to study device performances and to understand their working principle. E.g. it was used to shed light on the charge-discharge process of graphene-based energy storage devices (Share et al., 2016). Raman spectroscopy continues to be used for fundamental material studies (Cong et al., 2020).

Raman spectroscopy is a prime characterization techniques for all types of carbons and contributed significantly to the understanding of graphene and LMs. However, there are over 1800 exfoliable or potentially exfoliable LMs (Mounet et al., 2018), of which only a small fraction has been studied so far. Raman spectroscopy is already being used to characterize LMs beyond graphene and to study the interaction between different LMs in heterostructures in the high and low frequency range. E.g. Raman spectroscopy has been used to study magnetic ordering in magnetic LMs (Kim et al., 2019).

Other advanced Raman techniques such as coherent anti-Stokes Raman scattering (CARS) are emerging for the characterization of LMs (Virga et al., 2019). CARS is a non-linear optical process that exploits the interaction between two laser pulses and is used for imaging samples. As for conventional Raman scattering, the first laser beam 'pump', ω_p, will cause S-Raman scattering, ω_S, creating a phonon, Fig. 12. This phonon can then be used directly for an AS-Raman process under the condition that the correlated photon energies (ω_p) match (Virga et al., 2019), Fig. 12. During this process the interaction of laser pulses and sample results in the generation of vibrational coherences, i.e. the atoms oscillate with the same phase, which in turn can lead to a signal enhancement of several orders of magnitude (Virga et al., 2019). CARS is particularly interesting for biological research due to its marker free imaging and ability to suppress fluorescence that would otherwise overshadow the Raman signal of the sample (Begley et al., 1974).

Acknowledgments

We acknowledge funding from ERC grants GIPT, Hetero2D, GSYNCOR, EU Graphene Flagship, EU Grants Graph-X, GREENCAP, EIC grant CHARM, and EPSRC grants EP/X015742/1, EP/V000055/1, EP/N010345/1, EP/L016087/1, EP/P00119X/1.

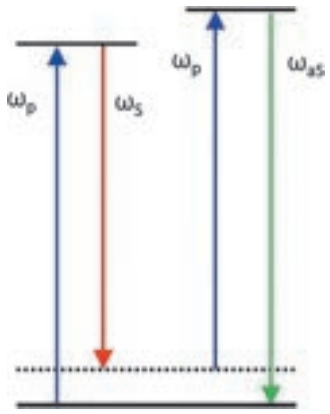

Fig. 12 Schematic of the coherent anti-Stokes Raman scattering process.

References

Ando T (2007) Magnetic oscillation of optical phonon in graphene. *Journal of the Physical Society of Japan* 76: 024712.

Backes C, Abdelkader AM, Concepción A, Andrieux-Ledier A, et al. (2020) Production and processing of graphene and related materials. *2D materials* 7: 022001.

Basko DM, Piscanec S, and Ferrari AC (2009) Electron-electron interactions and doping dependence of the two-phonon Raman intensity in graphene. *Physical Review B* 80: 165413.

Beams R, Cançado LG, and Novotny L (2011) Low temperature Raman study of the electron coherence length near graphene edges. *Nano Letters* 11: 1177–1181.

Begley RF, Harvey AB, and Byer RL (1974) Coherent anti-Stokes Raman spectroscopy. *Applied Physics Letters* 25: 387.

Bonaccorso F, Lombardo A, Hasan T, Sun Z, Colombo L, and Ferrari AC (2012) Production and processing of graphene and 2d crystals. *Materials Today* 15: 564–589.

Brüesch P (1986) *Phonons: Theory and Experiments II*. Springer.

Bruna M, Ott AK, Ijäs M, Yoon D, Sassi U, and Ferrari AC (2014) Doping dependence of the Raman spectrum of defected graphene. *ACS Nano* 8: 7432–7441.

Bunch JS, van der Zande AM, Verbridge SS, Frank IW, Tanenbaum DM, Parpia JM, Craighead HG, and McEuen PL (2007) Electromechanical resonators from graphene sheets. *Science* 315: 490–493.

Cançado LG, Jorio A, Ferreira EHM, Stavale F, Achete CA, Capaz RB, Moutinho MVO, Lombardo A, Kulmala TS, and Ferrari AC (2011) Quantifying defects in graphene via Raman spectroscopy at different excitation energies. *Nano Letters* 11: 3190–3196.

Cançado LG, Pimenta MA, Neves BRA, Dantas MSS, and Jorio A (2004) Influence of the atomic structure on the Raman spectra of graphite edges. *Physical Review Letters* 93: 247401.

Cao Y and Sun M (2022) Tip-enhanced Raman spectroscopy. *Reviews in Physics* 8: 100067.

Cardona M and Güntherodt G (1982) *Light Scattering in Solids II*. Springer.

Casiraghi C, Hartschuh A, Lidorikis E, Qian H, Harutyunyan H, Gokus T, Novoselov KS, and Ferrari AC (2007a) Rayleigh imaging of graphene and graphene layers. *Nano Letters* 7: 2711–2717.

Casiraghi C, Hartschuh A, Qian H, Piscanec S, Georgi C, Fasoli A, Novoselov KS, Basko DM, and Ferrari AC (2009) Raman spectroscopy of graphene edges. *Nano Letters* 9: 1433–1441.

Casiraghi C, Pisana S, Novoselov KS, Geim AK, and Ferrari AC (2007b) Raman fingerprint of charged impurities in graphene. *Applied Physics Letters* 91: 233108.

Cong X, Liu X-L, Lin M-L, and Tan P-H (2020) Application of Raman spectroscopy to probe fundamental properties of two-dimensional materials. *npj 2D Materials and Applications* 4: 13.

Das A, Pisana S, Chakraborty B, Piscanec S, Saha SK, Waghmare UV, Novoselov KS, Krishnamurthy HR, Geim AK, Ferrari AC, and Sood AK (2008) Monitoring dopants by Raman scattering in an electrochemically top-gated graphene transistor. *Nature Nanotechnology* 3: 210–215.

de Fazio D, Purdie DG, Ott AK, Braeuninger-Weimer P, Khodkov T, Goossens S, Taniguchi T, Watanabe K, Livreri P, Koppens FHL, Hofmann S, Goykhman I, Ferrari AC, and Lombardo A (2019) High-mobility, wet-transferred graphene grown by chemical vapor deposition. *ACS Nano* 13: 8926–8935.

Ding F, Ji H, Chen Y, Herklotz A, Dörr K, Mei Y, Rastelli A, and Schmidt OG (2010) Stretchable graphene: A close look at fundamental parameters through biaxial straining. *Nano Letters* 10: 3453–3458.

Dresselhaus MS, Dresselhaus G, and Eklund PC (1996) Raman scattering in fullerenes. *Journal of Raman Spectroscopy* 27: 351–371.

Dresselhaus MS, Dresselhaus G, Saito R, and Jorio A (2005) Raman spectroscopy of carbon nanotubes. *Physics Reports* 409: 47–99.

Faugeras C, Amado M, Kossacki P, Orlita M, Kühne M, Nicolet AAL, Latzshev YI, and Potemski M (2011) Magneto-Raman scattering of graphene on graphite: Electronic and phonon excitations. *Physical Review Letters* 107: 036807.

Faugeras C, Kossacki P, Basko DM, Amado M, Sprinkle M, Berger C, de Heer WA, and Potemski M (2010) Effect of a magnetic field on the two-phonon Raman scattering in graphene. *Physical Review B* 81: 155436.

Ferrari AC and Basko DM (2013) Raman spectroscopy as a versatile tool for studying the properties of graphene. *Nature Nanotechnology* 8: 235–246.

Ferrari AC, Meyer JC, Scardaci V, Casiraghi C, Lazzeri M, Mauri F, Piscanec S, Jiang D, Novoselov KS, Roth S, and Geim AK (2006) Raman spectrum of graphene and graphene layers. *Physical Review Letters* 97: 187401.

Ferrari AC and Robertson J (2000) Interpretation of Raman spectra of disordered and amorphous carbon. *Physical Review B* 61: 14095–14107.

Gadelha AC, Ohlberg DAA, Rabelo C, Neto EGS, Vasconcelos TL, Campos JL, Lemos JS, Ornelas V, Miranda D, Nadas R, Santana FC, Watanabe K, Taniguchi T, van Troeye B, Lamparski M, Meunier V, Nguyen V-H, Paszko D, Charlier J-C, Campos LC, Cançado LG, Medeiros-Ribeiro G, and Jorio A (2021) Localization of lattice dynamics in low-angle twisted bilayer graphene. *Nature* 590: 405–409.

Goerbig MO, Fuchs JN, Kechedzhi K, and Fal'ko VI (2007) Filling-factor-dependent magnetophonon resonance in graphene. *Physical Review Letters* 99: 087402.

Hartschuh A, Sánchez EJ, Xie XS, and Novotny L (2003) High-resolution near-field Raman microscopy of single-walled carbon nanotubes. *Physical Review Letters* 90: 095503.

Huang M, Yan H, Heinz TF, and Hone J (2010) Probing strain-induced electronic structure change in graphene by Raman spectroscopy. *Nano Letters* 10: 4074–4079.

Kalbac M, Reina-Cecco A, Farhat H, Kong J, Kavan L, and Dresselhaus MS (2010) The influence of strong electron and hole doping on the Raman intensity of chemical vapor-deposition graphene. *ACS Nano* 4: 6055–6063.

Kashuba O and Fal'ko VI (2012) Role of electronic excitations in magneto-Raman spectra of graphene. *New Journal of Physics* 14: 105016.

Kashuba O and Fal'ko VI (2009) Signature of electronic excitations in the Raman spectrum of graphene. *Physical Review B* 80: 241404.

Kim K, Lee J-U, and Cheong H (2019) Raman spectroscopy of two-dimensional magnetic van der Waals materials. *Nanotechnology* 30: 452001.

Kim Y, Ma Y, Imambekov A, Kalugin NG, Lombardo A, Ferrari AC, Kono J, and Smirnov D (2012) Magnetophonon resonance in graphite: High-field Raman measurements and electron-phonon coupling contributions. *Physical Review B* 85: 121403.

Kittel C (2005) *Introduction to Solid State Physics*. John Wiley and Sons, Inc.

Kneipp K, Moskovits M, and Kneipp H (2006) *Surface Enhanced Raman Scattering: Physics and Applications*. Springer.

Knight DS and White WB (1989) Characterization of diamond films by Raman spectroscopy. *Journal of Materials Research* 4: 385–393.

Kossacki P, Faugeras C, Kühne M, Orlita M, Nicolet AAL, Schneider JM, Basko DM, Latyshev YI, and Potemski M (2011) Electronic excitations and electron-phonon coupling in bulk graphite through Raman scattering in high magnetic fields. *Physical Review B* 84: 235138.

Krishnan RS and Narayanan PS (1950) Intensity ratio of the Raman lines in diamond. *Proceedings of the Indian Academy of Sciences - Section A* 32: 352.

Landsberg G and Mandelstam L (1928) Über die Lichtzerstreuung in Kristallen. *Zeitschrift für Physik* 50: 769–780.

Larmor J (1907) *Memoir and scientific correspondence of the late Sir George Gabriel Stokes*, 2 vols. Cambridge University Press.

Lee C, Wei X, Kysar JW, and Hone J (2008) Measurement of the elastic properties and intrinsic strength of monolayer graphene. *Science* 321: 385.

Lee J, Shim S, Kim B, and Shin HS (2011) Surface-enhanced Raman scattering of single- and few-layer graphene by the deposition of gold nanoparticles. *Chemistry – A European Journal* 17: 2381–2387.

Loudon R (1965) Theory of the resonance Raman effect in crystals. *Journal de Physique France* 26: 677–683.

Maiman TH (1960) Stimulated optical radiation in ruby. *Nature* 187: 493–494.

Malard LM, Lafeta L, Cunha RS, Nadas R, Gadelha A, Cançado LG, and Jorio A (2021) Studying 2D materials with advanced Raman spectroscopy: Cars, SRS and TERS. *Physical Chemistry Chemical Physics* 23: 23428–23444.

Metzger C, Rémi S, Liu M, Kusminskiy SV, Castro Neto AH, Swan AK, and Goldberg BB (2010) Biaxial strain in graphene adhered to shallow depressions. *Nano Letters* 10: 6–10.

Mie G (1908) On optical characteristics of turbid media, with special reference to colloid metallic solutions. *Ann. Phys.* 330: 377–445.

Mohiuddin TMG, Lombardo A, Nair RR, Bonetti A, Savini G, Jalil R, Bonini N, Basko DM, Galiotis C, Marzari N, Novoselov KS, Geim AK, and Ferrari AC (2009) Uniaxial strain in graphene by Raman spectroscopy: *G* peak splitting, Grüneisen parameters, and sample orientation. *Physical Review B* 79: 205433.
Mohr M, Maultzsch J, and Thomsen C (2010) Splitting of the Raman 2D band of graphene subjected to strain. *Physical Review B* 82: 201409.
Mounet N, Gibertini M, Schwaller P, Campi D, Merkys A, Marrazzo A, Sohier T, Castelli IE, Cepellotti A, Pizzi G, and Marzari N (2018) Two-dimensional materials from high-throughput computational exfoliation of experimentally known compounds. *Nature Nanotechnology* 13: 246–252.
Mucha-Kruczyński M, Kashuba O, and Fal'ko VI (2010) Spectral features due to inter-Landau-level transitions in the Raman spectrum of bilayer graphene. *Physical Review B* 82: 045405.
Nemanich RJ, Lucovsky G, and Solin SA (1977) Infrared active optical vibrations of graphite. *Solid State Communications* 23: 117–120.
Novoselov KS, Geim AK, Morozov SV, Jiang D, Zhang Y, Dubonos SV, Grigorieva IV, and Firsov AA (2004) Electric field effect in atomically thin carbon films. *Science* 306: 666–669.
Piscanec S, Lazzeri M, Mauri F, Ferrari AC, and Robertson J (2004) Kohn anomalies and electron-phonon interactions in graphite. *Physical Review Letters* 93: 185503.
Pizzi G, Milana S, Ferrari AC, Marzari N, and Gibertini M (2021) Shear and breathing modes of layered materials. *ACS Nano* 15: 12509–12534.
Placzek G (1934) *Rayleigh-Streuung und Raman-Effect*. Leipzig: Akademische Verlagsgesellschaft.
Pocsik I, Hundhausen M, Koos M, and Ley L (1998) Origin of the D peak in the Raman spectrum of microcrystalline graphite. *Journal of Non-Crystalline Solids* 227: 1083–1086.
Proctor JE, Gregoryanz E, Novoselov KS, Lotya M, Coleman JN, and Halsall MP (2009) High-pressure Raman spectroscopy of graphene. *Physical Review B* 80: 073408.
Purdie DG, Pugno NM, Taniguchi T, Watanabe K, Ferrari AC, and Lombardo A (2018) Cleaning interfaces in layered materials heterostructures. *Nature Communications* 9: 5387.
Rabelo C, Vasconcelos TL, Publio BC, Miranda H, Cançado LG, and Jorio A (2020) Linkage between micro- and nano-Raman spectroscopy of defects in graphene. *Physical Review Applied* 14: 024056.
Raman CV and Krishnan KS (1928) A new type of secondary radiation. *Nature* 121: 501–502.
Schawlow AL and Townes CH (1958) Infrared and optical masers. *Physical Review* 112: 1940–1949.
Schedin F, Lidorikis E, Lombardo A, Kravets VG, Geim AK, Grigorenko AN, Novoselov KS, and Ferrari AC (2010) Surface-enhanced Raman spectroscopy of graphene. *ACS Nano* 4: 5617–5626.
Share K, Cohn AP, Carter RE, and Pint CL (2016) Mechanism of potassium ion intercalation staging in few layered graphene from in situ Raman spectroscopy. *Nanoscale* 8: 16435–16439.
Smekal A (1923) Zur Quantentheorie der Dispersion. *Naturwissenschaften* 11: 873–875.
Stöckle RM, Suh YD, Deckert V, and Zenobi R (2000) Nanoscale chemical analysis by tip-enhanced Raman spectroscopy. *Chemical Physics Letters* 318: 131–136.
Strutt JW Lord Rayleigh (1871) On the light from the sky, its polarization and colour. *Philosophical Magazine* 41: 274.
Tan PH, Han WP, Zhao WJ, Wu ZH, Chang K, Wang H, Wang YF, Bonini N, Marzari N, Pugno N, Savini G, Lombardo A, and Ferrari AC (2012) The shear mode of multilayer graphene. *Nature Materials* 11: 294–300.
The Nobel Prize (2022) *The Nobel Prize in Physics 1930: Sir Chandrasekhara Venkata Raman*. https://www.nobelprize.org/prizes/physics/1930/raman/facts/. [Accessed].
Thomsen C and Reich S (2000) Double resonant Raman scattering in graphite. *Physical Review Letters* 85: 5214–5217.
Tuinstra F and Koenig JL (1970) Raman spectrum of graphite. *The Journal of Chemical Physics* 53: 1126–1130.
Virga A, Ferrante C, Batignani G, De Fazio D, Nunn ADG, Ferrari AC, Cerullo G, and Scopigno T (2019) Coherent anti-stokes Raman spectroscopy of single and multi-layer graphene. *Nature Communications* 10: 3658.
Wallace PR (1947) The band theory of graphite. *Physical Review* 71: 622–634.
Yoon D, Son Y-W, and Cheong H (2011) Strain-dependent splitting of the double-resonance Raman scattering band in graphene. *Physical Review Letters* 106: 155502.
Yu PY and Cardona M (1996) *Fundamentals of Semiconductors: Physics and Material Properties*. Springer.
Zabel J, Nair RR, Ott A, Georgiou T, Geim AK, Novoselov KS, and Casiraghi C (2012) Raman spectroscopy of graphene and bilayer under biaxial strain: Bubbles and balloons. *Nano Letters* 12: 617–621.
Zhang X, Han WP, Wu JB, Milana S, Lu Y, Li QQ, Ferrari AC, and Tan PH (2013) Raman spectroscopy of shear and layer breathing modes in multilayer MoS_2. *Physical Review B* 87: 115413.
Zhao W, Tan PH, Liu J, and Ferrari AC (2011) Intercalation of few-layer graphite flakes with $FeCl_3$: Raman determination of Fermi level, layer by layer decoupling, and stability. *Journal of the American Chemical Society* 133: 5941–5946.